Journal of Power Sources 549 (2022) 232048

Contents lists available at ScienceDirect

Journal of Power Sources

journal homepage: www.elsevier.com/locate/jpowsour

Redox-stable composite electrodes for CH_4 conversion reactors based on proton ceramic electrochemical cells

L. Almar [1], N. Bausá [1], M. Fabuel, S. Escolástico [**], J.M. Serra [*]

Instituto de Tecnología Química (Universitat Politècnica de València – Consejo Superior de Investigaciones Científicas), Av. Los Naranjos, s/n, 46022, Valencia, Spain

HIGHLIGHTS

- Various redox-stable backbone materials were studied on protonic electrolytes.
- Operation enabled alternating between air and non-oxidative hydrocarbon/H_2-rich atmospheres.
- Catalytically-adjusted electrodes for protonic cells very active under redox-cycling.
- LSM/BCZY27+Pt/CeO_2 showed the lowest R_p at 700 °C, i.e., 0.7 Ω cm^2 in CH_4/H_2.

ABSTRACT

Electrochemical reactors based on proton-conducting ceramic electrolytes show a great potential in the conversion of hydrocarbons by enabling the intensification via the in-situ extraction of the H_2 produced. However, non-oxidative operation conditions lead to the progressive coke formation on the catalyst and electrodes and thus, an oxidative regeneration cycle is required to restore the catalyst activity. Consequently, newly redox-stable electrodes are required to enable operation under both non-oxidative H_2-extraction and coke-oxidation conditions. Here, four composite materials were investigated as redox-stable electrode backbones for their integration in proton-conducting cells, composed by the proton conductor $BaCe_{0.2}Zr_{0.7}Y_{0.1}O_{3-\delta}$ (BCZY27) and $La_{0.85}Sr_{0.15}FeO_3$ (LSF8515), $La_{0.5}Sr_{0.5}FeO_3$ (LSF55), $La_{0.84}Sr_{0.16}Cr_{0.5}Mn_{0.5}O_3$ (LSCM) or $La_{0.8}Sr_{0.2}MnO_3$ (LSM). Chemical compatibility with the electrolyte and electrochemical performance were characterized in the range 500–800 °C. LSCM/BCZY27 and LSM/BCZY27 showed the best performance. The electrode activity was boosted by catalytically activating with Pt and CeO_2 nanoparticles while exhibiting outstanding stability upon redox cycling. LSM/BCZY27+Pt/CeO_2 showed the lowest polarization resistance, i.e., achieving 0.7 Ω cm^2 at 700 °C in 10% CH_4 and 9% H_2 and 0.14 Ω cm^2 in air, revealing a high potential as redox-stable electrode for non-oxidative hydrocarbon conversion in electrochemical reactors.

1. Introduction

Interest about proton-conducting oxides has grown in the last years due to their potential applications such as fuel cells for energy conversion and storage, electrolyzers for hydrogen production and electrochemical reactors. Process intensification and pure on-site hydrogen production using hydrogen-selective membranes have been highlighted in different studies [1–4]. Malerød-Fjeld et al. [5] used a $BaZrO_3$-based proton-conducting electrolyte to demonstrate an electrochemically driven protonic methane reformer (PMR). Another key technology for CH_4 is non-oxidative methane dehydroaromatization (MDA: $6CH_4 \leftrightarrow C_6H_6 + 9H_2$), allowing exploitation of natural gas reserves by direct conversion into transportable liquids. Morejudo et al. [6] demonstrated $BaZrO_3$-based protonic ceramic membrane as a promising alternative giving rise to high aromatic yields and improved catalyst stability compared to the conventional reactors [7–9]. Another important reaction type related with the CH_4 upgraded and dehydrogenation of olefins can be performed in this kind of reactors [3]. Some of these reactions are prone to produce coke that provokes the catalyst deactivation and loss of the electrode performance. Coke deactivation can be mitigated by re-oxidizing or burning-off the carbon depositions. For this purpose, the electrodes should be redox stable operating reversibly in both fuel and oxygen containing atmospheres. Redox-stable electrodes offer also the opportunity to work as a reversible electrochemical cell that can operate in both modes (1) pumping or electrolysis mode to convert the excess of electrical energy to chemical energy and (2) fuel cell mode to convert chemical energy to electricity, allowing the balance electricity demand and supply of intermittent renewable energy. Redox electrodes must

* Corresponding author.
** Corresponding author.
E-mail addresses: soesro@itq.upv.es (S. Escolástico), jmserra@itq.upv.es (J.M. Serra).
[1] Both authors contributed equally.

https://doi.org/10.1016/j.jpowsour.2022.232048
Received 23 June 2022; Received in revised form 11 August 2022; Accepted 29 August 2022
Available online 23 September 2022

fulfil important requirements, i.e., (i) high electronic conductivity under both oxidizing and reducing atmospheres, (ii) high electrocatalytic activity for the oxygen (OER and ORR) and the hydrogen (HER and HOR) evolution and reduction/oxidation reactions and (iii) negligible Thermal Expansion Coefficients (TEC) change in a wide range of oxygen partial pressures to avoid delamination or cracks upon redox cycling.

Only few studies related with redox-stable electrodes for protonic ceramic electrochemical cells (PCECs) can be found in literature. $BaZr_{0.1}Co_{0.4}Fe_{0.4}Y_{0.1}O_{3-\delta}$ (BZCFY) has been proposed as redox-stable electrode, however, important polarization resistance was observed under reducing atmospheres due to the phase structure decomposition [10]. $PrBaFe_2O_{5+\delta}$ has been recently reported as a promising redox-stable electrode due to its redox-cycling stability (H_2-air cycles) [11]. In addition, protonic cells symmetrically designed with (Nd,Ba)FeO_3 electrodes showed operational effectiveness under both oxidizing and reducing conditions [12].

Most developments about reversible redox-stable electrodes have been performed in the frame of the reversible solid oxide electrochemical cells (ReSOECs). Main research on redox electrodes is based on materials such as Sr- and Ca-doped $LaCrO_3$ perovskites and Mn-doped $LaCrO_3$ based materials that exhibit high electrical conductivities in air [13–16]. A symmetrical cell with a $La_{0.75}Sr_{0.25}Cr_{0.5}Mn_{0.5}O_{3-\delta}$ electrode was developed to operate in both fuel cell and electrolysis modes by Bastidas et al. [17] demonstrating their efficiency and redox stability. Graves et al. [18] observed that the composite electrode LSM/YSZ (LSM: Sr-doped $LaMnO_3$) can operate in reversible mode without suffering any degradation, in contrast with the degradation observed under constant electrolysis conditions. In previous works, compatibility of $La_{0.8}Sr_{0.2}MnO_3$ (LSM), $La_{0.6}Sr_{0.4}Co_{0.2}Fe_{0.8}O_{3-\delta}$ (LSCF) and $Ba_{0.5}Sr_{0.5}Co_{0.8}Fe_{0.2}O_{3-\delta}$ (BSCF) with the protonic material BCZY27 was demonstrated [19]. LSM and LSCF showed a promising performance as steam electrode. In addition, performance of the LSM electrode was further improved by catalytic infiltration [20,21]. In fact, during the last decade, many efforts were devoted to promote the catalytic activity of the electrodes while retaining the constituent materials properties with a wide range infiltration approaches [22–24]. Surface modification and catalytic activation by infiltration is meaningful for most applications inducing new ionic/electronic pathways on the electrodes surface and improving the overall catalytic processes, due to the larger surface area and increased number of reaction sites available originated by well disperse nanoparticles [20,25,26].

Based on the above investigations, our motivation was to explore different composite electrodes that can act as redox stable electrodes for CH_4 conversion reactions in protonic ceramic electrochemical cells (PCECs). In this paper, we study the compatibility and electrochemical performance of four candidate electrodes composed by different perovskite materials with the protonic $BaCe_{0.2}Zr_{0.7}Y_{0.1}O_{3-\delta}$ (BCZY27) in H_2 and CH_4 atmospheres. After that, the best performing composites LSCM/BCZY27 and LSM/BCZY27 are catalytically activated by nanoparticles' infiltration and study as redox-stable electrodes. The infiltrated LSM/BCZY27 electrode with Pt and CeO_2 shows the lowest polarization resistances and is redox stable in both oxidizing and reducing atmospheres.

2. Experimental

Redox-stable electrodes were fabricated by mixing four different perovskite phases with the proton conductor $BaCe_{0.2}Zr_{0.7}Y_{0.1}O_{3-\delta}$ (BCZY27). The selected four materials were: $La_{0.85}Sr_{0.15}FeO_3$ (LSF8515), $La_{0.5}Sr_{0.5}FeO_3$ (LSF55), $La_{0.8}Sr_{0.2}Cr_{0.5}Mn_{0.5}O_3$ (LSCM) and $La_{0.8}Sr_{0.2}MnO_3$ (LSM). The perovskite powders were prepared by different methods. LSF8515 and LSF55 were synthesized by complexation–gelation processes followed by final controlled pyrolysis (Pechini method) and sintered at 1000 °C for 8 h. Commercial powders of LSCM (Marion technologies) and LSM (Marion technologies) were employed.

The chemical compatibility of the abovementioned materials with 50 vol % BCZY27 was studied by X-ray diffraction (XRD). Commercial BCZY27 powder (Cerpotech) was sintered at 1300 °C before the compatibility tests. Both phases (BCZY27 and the corresponding perovskite phase) were ball-milled with a final calcination step specifically for LSF8515, LSF55 at 1000 °C and LSCM, and LSM at 1100 °C. XRD was performed in a CubiX FAST equipment using $CuK\alpha_{1,2}$ radiation and an X'Celerator detector in Bragg-Brentano geometry in the 2θ range from 20 to 70°. The obtained XRD patterns were analyzed using X'Pert Highscore Plus software (PANalytical).

The selected electrodes were prepared by mixing 50 vol % of each

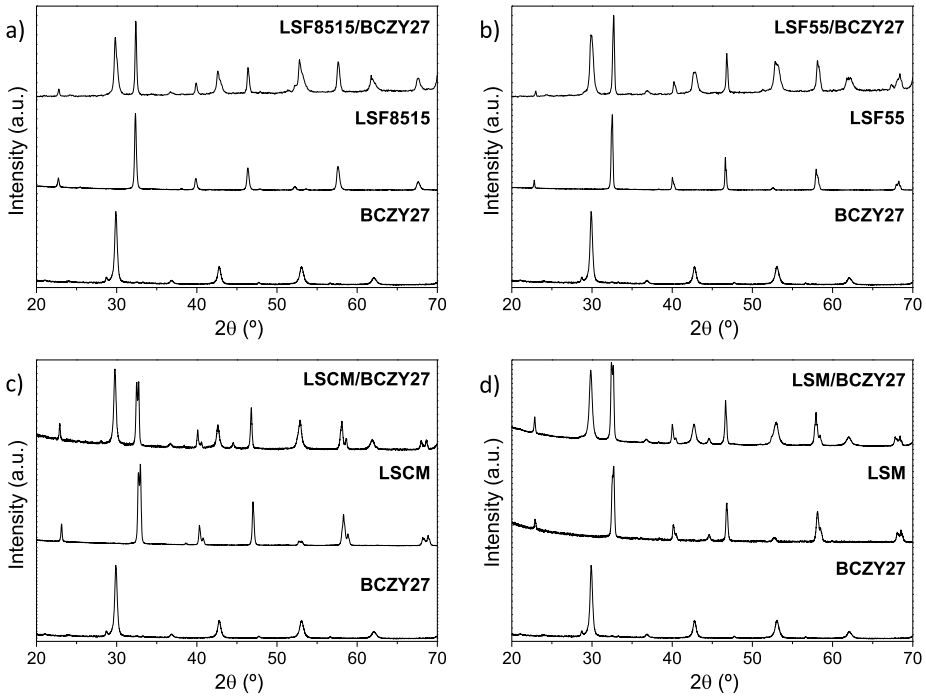

Fig. 1. XRD patterns to study the chemical compatibility of the composites: LSF8515/BCZY27 (a), LSF55/BCZY27 (b), LSCM/BCZY27 (c) and LSM/BCZY27 (d).

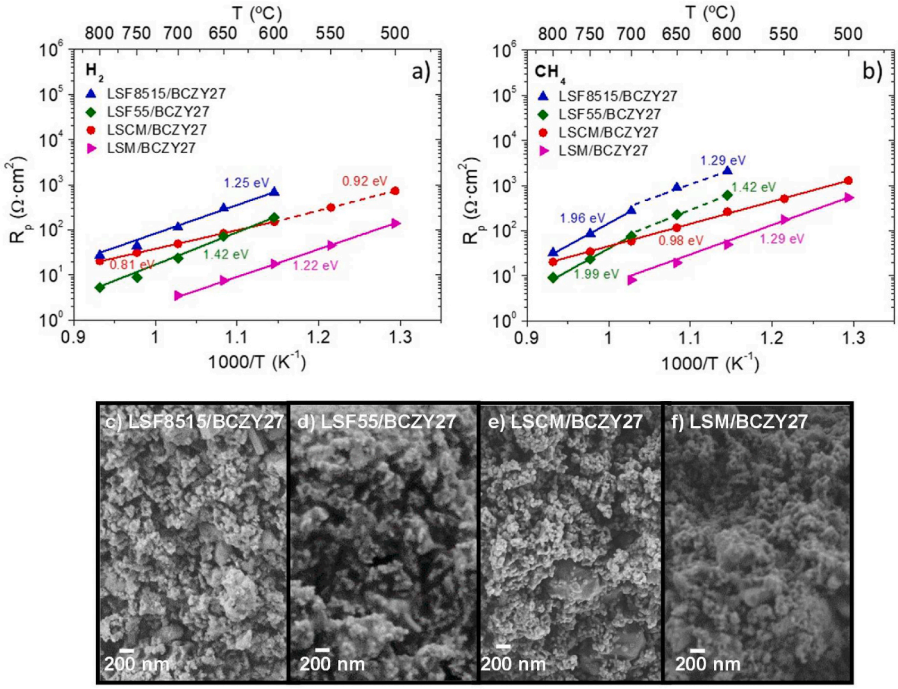

Fig. 2. Total polarization resistance for the composite electrodes LSF8515/BCZY27, LSF55/BCZY27, LSCM/BCZY27 and LSM/BCZY27 measured in symmetrical cells as a function of temperature under humidified atmospheres composed of 50% H_2 in Ar (a) and 9% CH_4 -10% H_2 in Ar (b). SEM images of the composite electrodes LSF8515/BCZY27 (c), LSF55/BCZY27 (d), LSCM/BCZY27 (e) and LSM/BCZY27 (f) after the electrochemical measurements.

phase (BCZY27 as protonic phase and LSF8515, LSF55, LSCM or LSM as electronic phase). Symmetrical cells were fabricated by screen-printing the electrode inks onto both sides of BCZY27 dense electrolyte pellets with an electrode active area of 0.64 cm^2. Inks were prepared by using terpineol and ethylcellulose in a three-roll mill. The sintering temperature of the electrodes was 1000 °C for LSF8515/BCZY27 and LSF55/BCZY27 and 1100 °C for LSCM/BCZY27 and LSM/BCZY27. Gold paste was screen-printed as a mesh on top of the composite electrodes to ensure proper current collection.

In addition, LSCM/BCZY27 and LSM/BCZY27 electrodes were infiltrated with CeO_2, Pt and Pt/CeO_2 precursors to improve their catalytic activity. Solutions (ethanol-water) with adjusted surface tension were prepared, containing 0.15 M tetraammineplatinum (II) nitrate (Sigma Aldrich) and 2 M cerium (III) nitrate hexahydrate (Sigma Aldrich). The solution was dropped over the whole electrode surfaces and calcined at 800 °C to obtain the respective oxides/metals (CeO_2, Pt, and Pt/CeO_2). In the case of the electrodes infiltrated with Pt/CeO_2, first the Pt solution was dropped over the electrode followed by a thermal treatment at 800 °C. Then, the Ce solution was dropped and the sample was calcined at 800 °C.

The electrochemical performance and reversibility of the fabricated cells were evaluated by electrochemical impedance spectroscopy (EIS) with a Solartron Analytical 1470E CellTest System frequency response analyzer in the 0.03–10 Hz frequency range [6]. The sintered cells were placed in a quartz reactor between Pt meshes and tested in a temperature range between 800 °C and 500 °C and humidified (3% H_2O) reducing atmospheres: (a) 50% H_2-50% Ar and (b) 9% CH_4-10% H_2-81% Ar with a total flow rate of 50 mL min^{-1} at each electrolyte side. Additionally, best performance materials were tested in humidified synthetic air and redox cycles (humidified synthetic air – humidified 50% H_2 in Ar). The three-wire configuration was used to analyze the EIS under the applied current (bias). By using this configuration, only one electrode contribution is measured enabling the study of the current density effect. The collected impedance data was analyzed and fit using the ZView software.

The microstructure of the electrodes and the interface electrode-electrolyte was investigated by Field-emission scanning electron microscopy (FE-SEM) (Zeiss Ultra 55). Finally, the capability of forming coke was evaluated for BZCY, LSM and LSCM under CH_4 and aromatics containing atmospheres. Powder materials were treated at 800 °C in pure CH_4 saturated in toluene for 1 h. Subsequently, thermogravimetric (TGA) analysis was performed in synthetic air up to 1000 °C to quantify the carbonaceous deposits formed on the materials during the treatment.

3. Results

3.1. Chemical compatibility of the composite materials

Composite electrodes were developed to enable thermal expansion coefficient (TEC) matching between the electrolyte and the electrode, as the four selected electrode materials have a higher TEC, ranging from $9.3{\cdot}10^{-6}$ K^{-1} for LSCM to $19.6{\cdot}10^{-6}$ K^{-1} for LSF55 [27–29], than BCZY27 ($8.76{\cdot}10^{-6}$ K^{-1}) [30].

Fig. 1 shows the XRD patterns of the single compounds (LSF8515, LSF55, LSCM, LSM and BCZY27) and the developed composites. LSF8515 and LSF55 were synthesized by Pechini and showed a perovskite structure with rhombohedral symmetry as observed in Fig. 1a and b. The composites LSF8515/BCZY27 and LSF55/BCZY27 showed compatibility of LSF8515 and LSF55 with BCZY27 as inferred by the XRD analysis, where no secondary phases are detected. For their fabrication, LSF8515 and LSF55 (pre-sintered at 1000 °C) were mixed with BCZY27 and subsequently calcined at 1000 °C for 5 h. Also, LSCM and LSM commercial powders present a single perovskite structure as can be observed in Fig. 1c–e. For the composite LSCM/BCZY27, LSCM (pre-sintered at 1100 °C) was mixed with BCZY27 and calcined at 1100 °C for 5 h. The XRD patterns showed only the two single perovskite phases related to both parent materials (Fig. 1c). The XRD pattern of LSM/BCZY27 in Fig. 1d shows all peaks associated to either LSM or BCZY27 while no secondary phases are detected. For the fabrication, LSM (sintered at 1100 °C) was mixed with BCZY27 and fired at 1100 °C for 5 h.

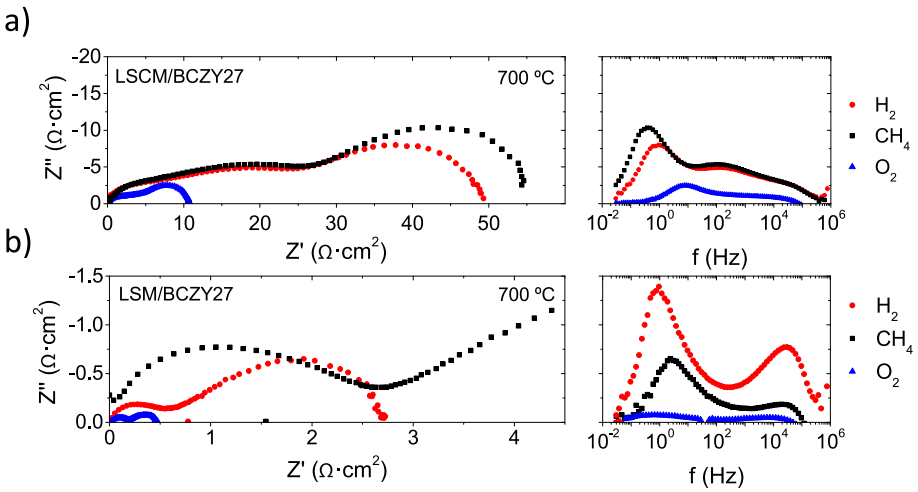

Fig. 3. EIS spectra (Nyquist and Bode plot) for the composite electrode LSCM/BCZY27 (a) and LSM/BCZY27 (b) at 700 °C measured under three different humidified atmospheres: 100% synthetic air (O_2), 50% H_2 in Ar (H_2) and 9% CH_4-10% H_2 in Ar (CH_4 containing atmospheres). Ohmic resistances were subtracted for clarity reasons.

3.2. Electrochemical characterization of the redox composite candidates

The electrochemical performance of the electrodes LSF8515/BCZY27, LSF55/BCZY27, LSCM/BCZY27 and LSM/BCZY27 was studied in symmetrical cells by impedance spectroscopy (EIS) acquired in a temperature range between 800 °C and 500 °C under two different atmospheres: 50% H_2-50% Ar and 9% CH_4-10% H_2-81% Ar, both saturated in water at 25 °C (3% H_2O).

Fig. 2 shows the Arrhenius plot for the total polarization resistance (R_p) contribution as a function of the temperature of the electrodes in

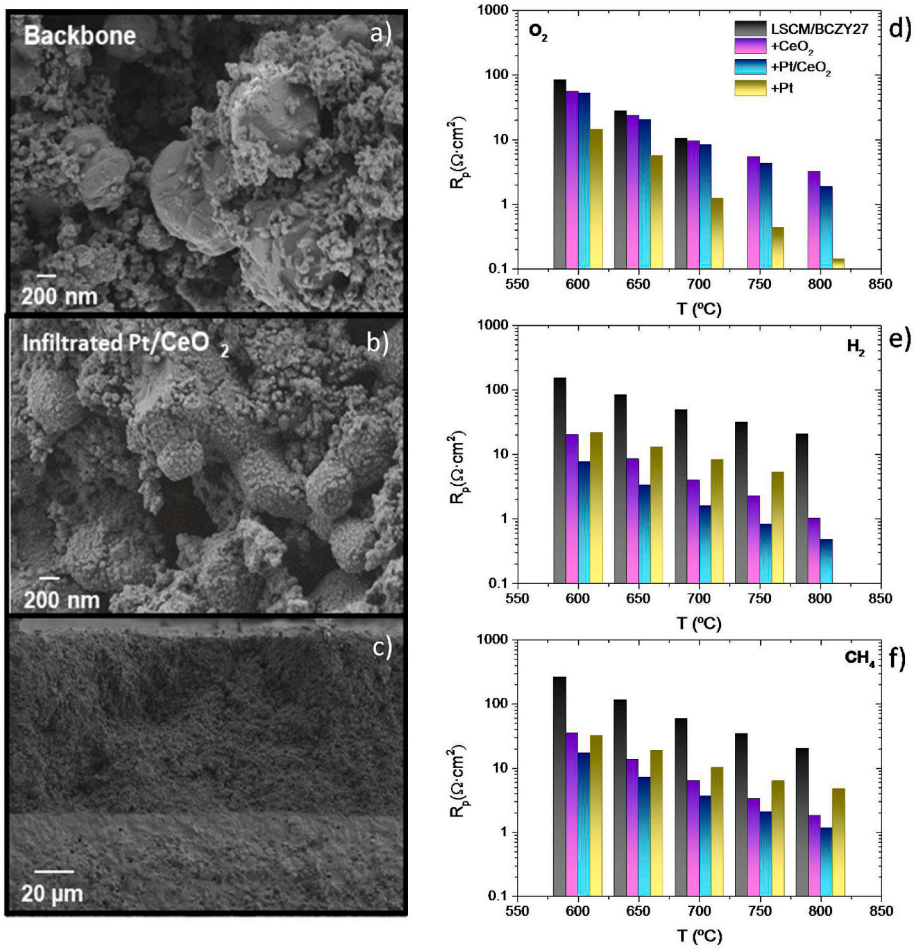

Fig. 4. SEM cross-sectional images of the backbone LSCM/BCZY27 (a) and of LSCM/BCZY27 infiltrated with Pt/CeO_2 (b,c). Total polarization resistance for the composite electrode LSCM/BCZY27 and LSCM/BCZY27 infiltrated with CeO_2, Pt and Pt/CeO_2 measured in symmetrical cells as a function of temperature under humidified synthetic air (d), 50% H_2 in Ar (e) and 9% CH_4-10% H_2 in Ar (f).

the symmetrical cells. In both atmospheres, LSM/BCZY27 electrode presents the best performance, exhibiting a polarization resistance at 700 °C of 3.27 Ω cm^2 and 8.10 Ω cm^2 in H_2 and CH_4–H_2, respectively. The maximum temperature tested for LSM/BCZY27 was 700 °C since LSM presents redox instability at high temperatures whereas is stable in reducing atmospheres below 800 °C [31]. This low polarization resistance could be related to the higher total conductivity of LSM under reducing atmospheres compared to LSCM, almost one order of magnitude higher [32]. The R_p values of LSF55/BCZY27 are lower than those of LSCM/BCZY27 at temperatures above 600–700 °C, whereas the latter presents better performance at lower temperatures due to its lower activation energy in both H_2 and CH_4–H_2. The lowest performance is observed for LSF8515/BCZY27 in both tested atmospheres. The lower performance of LSF8515 compared to LSF55 agrees with previous studies reporting a maximum in the total conductivity of $La_{1-x}Sr_xFeO_{3-\delta}$ for a Sr-content of x = 0.5 [33].

The activation energies (E_a) of the La-ferrite based electrodes present a similar trend in both atmospheres. A higher value is observed than for LSCM/BCZY27 and LSM/BCZY27 in H_2, while in CH_4–H_2 showed a two-fold behavior with a much higher E_a at higher temperatures, evidencing a change in the rate limiting step at 700 °C. LSCM/BCZY27 presents the lowest E_a values and similar in both atmospheres (0.81–0.96 eV) while for LSM/BCZY27 are between 1.22 and 1.29 eV.

SEM cross-sectional images of the LSF8515/BCZY27, LSF55/BCZY27, LSCM/BCZY27 and LSM/BCZY27 electrodes after the electrochemical measurements are shown in Fig. 2c–f to verify if degradation in the microstructure of the electrodes may occur after exposition to H_2 and CH_4 atmospheres. All the electrodes showed a similar morphology with particle sizes of ca. 100–500 nm and good interconnection between the two phases. No large coarsening or microstructural changes were observed regardless of the route followed to prepare the different perovskites.

Mixed conducting Sr-doped $LaFeO_3$ materials have been widely used as SOFC cathodes and as membrane materials for the partial oxidation of methane owing to the high electronic conduction, the stability in reducing atmospheres and the good electro-catalytic properties [34,35]. In this work, chemical compatibility with the protonic phase BCZY27 was proved in an attempt to work as redox-stable electrodes in chemical reactions where coke is produced and catalysts should be regenerated. However, no further studies were made with La-ferrite composites (LSF8515/BCZY27 and LSF55/BCZY27) because both showed lower electrochemical performance in the reducing atmospheres than the other tested composites.

LSM and LSCM-based composites presented the best performance among the tested electrodes and, therefore, they were selected for the redox stability studies. The symmetrical cells were further characterized by EIS under humidified synthetic air (O_2 containing atmosphere) as shown Fig. 3a and b at 700 °C. Polarization resistance values of 10.41 Ω cm^2 and 1.85 Ω cm^2 were obtained for LSCM/BZCY27 and LSM/BZCY27, respectively.

The impedance spectra of the electrodes were fitted to the equivalent circuit $LR_0(R_{HF}CPE_{HF})(R_{MF}CPE_{MF})(R_{LF}CPE_{LF})$. The total polarization resistance of the cathodes was calculated by the sum $R_p = R_{HF} + R_{MF} + R_{LF}$. Typical impedance spectra (Nyquist and Bode plots) recorded at 700 °C for LSCM/BCZY27 and LSM/BCZY27 are shown in Fig. 3a and b, respectively. From these graphs at least two different contributions can be distinguished. It seems that the contributions in the low and medium frequency range (LF + MF) with frequencies of 10 Hz and 100 Hz, respectively, and capacitances of 10^{-1}-10^{-2} F/cm^2, limit the performance of the composite electrodes at 700 °C under both H_2 and CH_4 containing atmospheres. LF and MF contributions can be related to elementary reactions at the electrodes surface, i.e. adsorption and dissociation of gas molecules (surface exchange kinetics). The contribution at high frequencies (HF), above 1 kHz (C = 10^{-6}-10^{-7} F/cm^2), seems to be lower compared to the LF + MF contributions and independent of the gas for LSCM/BCZY27, HF processes are usually associated to protonic and electronic losses at the electrode-electrolyte or the electrode-current collector interface.

Table 1
Polarization resistance (R_p) and activation energy (E_a) at 700 °C of LSCM/BCZY27, LSM/BCZY27 electrodes and LSCM/BCZY27, LSM/BCZY27 electrodes infiltrated with CeO_2, Pt y Pt/CeO_2 measured under humidified synthetic air, 50% H_2 in Ar and 9% CH_4-10% H_2 in Ar.

	R_p (Ω·cm^2) a 700 °C			E_a (eV)		
	Air	50% H_2	9% CH_4-10% H_2	Air High T (Low T)	50% H_2	9% CH_4-10% H_2
LSCM/BCZY27	10.41	49.22	58.79	1.53 (1.06)	0.91	0.98
LSCM/BCZY27 + CeO_2	9.56	3.94	6.38	1.25	1.11	1.26
LSCM/BCZY27 + Pt	1.22	8.15	10.21	1.49	0.73	0.81
LSCM/BCZY27 + Pt/CeO_2	8.29	1.59	3.69	1.31	1.11	0.95
LSM/BCZY27	1.85	3.51	8.10	1.17	1.22	1.29
LSM/BCZY27 + CeO_2	0.53	1.58	2.48	1.55 (1.20)	1.30	1.51
LSM/BCZY27 + Pt	0.14	2.53	7.57	1.77 (1.71)	0.64	0.74
LSM/BCZY27 + Pt/CeO_2	0.14	0.19	0.70	1.59 (1.36)	1.05	0.90

3.3. Electrocatalytic activation by infiltration and redox stability studies

In order to improve the electrocatalytic performance of the best performing LSM and LSCM-based electrodes, infiltration was made with different electrocatalysts i.e. CeO_2, Pt and Pt/CeO_2. Fig. 4 shows cross-sectional SEM images of the LSCM/BCZY27 backbone (Fig. 4a) and Pt/CeO_2 infiltrated LSCM/BCZY27 electrode layer (Fig. 4 b-c) after the electrochemical measurements. The CeO_2 and Pt nanoparticles showed a round shape and sizes range from 20 to 40 nm. The porous electrode layers showed good attachment onto the BCZY27 electrolyte. The thickness of the electrodes was around 60 μm with infiltrated nanoparticles homogenously dispersed throughout the electrode surface and no coarsening was observed after the electrochemical characterization, including redox stability cycles.

The effect of the catalyst infiltration on the performance was studied by EIS for both best performing cells LSCM/BCZY27/LSCM and LSM/BCZY27/LSM, from 800 to 500 °C under O_2, H_2 and CH_4 containing atmospheres, saturated in water at 25 °C (3% H_2O). Fig. 4d–f shows the polarization resistance values obtained for the composite LSCM/BCZY27 and LSCM/BCZY27 infiltrated with CeO_2, Pt and Pt/CeO_2 under the different tested conditions. The performance of all the infiltrated electrodes improved compared to the backbone LSCM/BCZY27 under all tested conditions. Particularly, LSCM/BCZY27 infiltrated with Pt/CeO_2 showed the lowest polarization resistance values of 1.59 and 3.69 Ω cm^2 at 700 °C under 50% H_2 and 9% CH_4-10% H_2 in Ar, respectively, and LSCM/BCZY27 infiltrated with Pt showed the lowest R_p of 1.22 Ω cm^2 at 700 °C under synthetic air. The LSCM/BCZY27 backbone and infiltrated with Pt showed lower R_p values under oxidizing conditions, while the electrodes infiltrated with CeO_2 and Pt/CeO_2 showed higher electrochemical performance in reducing atmospheres. All the polarization resistance values at 700 °C and activation energies are shown in Table 1.

The Pt-infiltrated LSCM/BCZY27 electrode presents the lowest activation energy (E_a) under H_2 and CH_4 atmospheres, and the highest E_a under synthetic air, when compared to the backbone and to the other infiltrated electrodes. Assuming that electrode backbones are identical, these changes can be correlated with the catalytic promotion with CeO_2, Pt and Pt/CeO_2 nanoparticles.

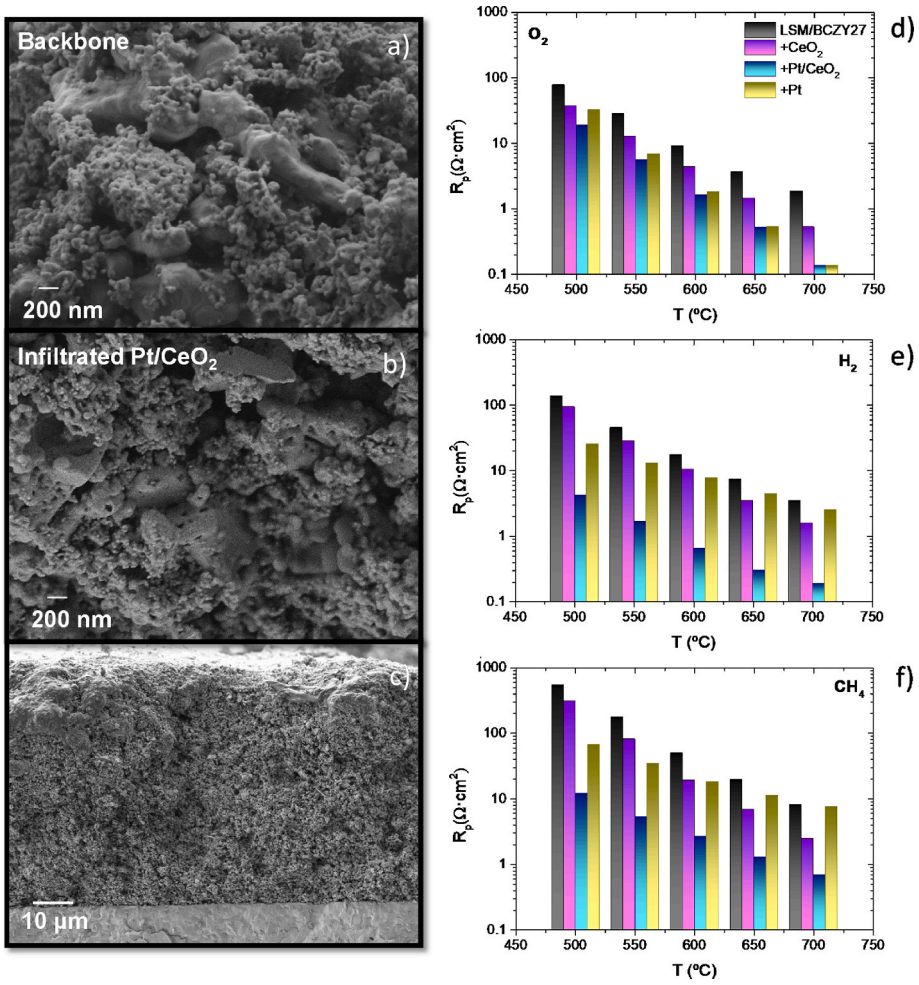

Fig. 5. SEM cross-sectional images of the backbone LSM/BCZY27 (a) and of LSM/BCZY27 infiltrated with Pt/CeO_2 (b,c). Total polarization resistance for the composite electrode LSM/BCZY27 (a) and LSM/BCZY27 infiltrated with CeO_2, Pt and Pt/CeO_2 measured in symmetrical cells as a function of temperature under humidified synthetic air (a), 50%H_2 in Ar (b) and 9% CH_4-10% H_2 in Ar (c).

Representative cross-sectional SEM images of the LSM/BCZY27 backbone and Pt/CeO_2 infiltrated LSM/BCZY27 electrode layers are shown in Fig. 5a–c. The catalyst nanoparticles are homogeneously dispersed on the porous-backbone surface and no coarsening after testing under all operational conditions.

Fig. 5d–f shows the polarization resistance values obtained for the LSM/BCZY27 backbone and LSM/BCZY27 infiltrated with CeO_2, Pt and Pt/CeO_2 in the different tested atmospheres. The electrochemical performance of all the infiltrated electrodes improved compared to the LSM/BCZY27 without infiltration under all tested conditions, due to the larger surface area and the improved surface-reaction kinetics. In general, better electrochemical performance is observed in an oxidizing

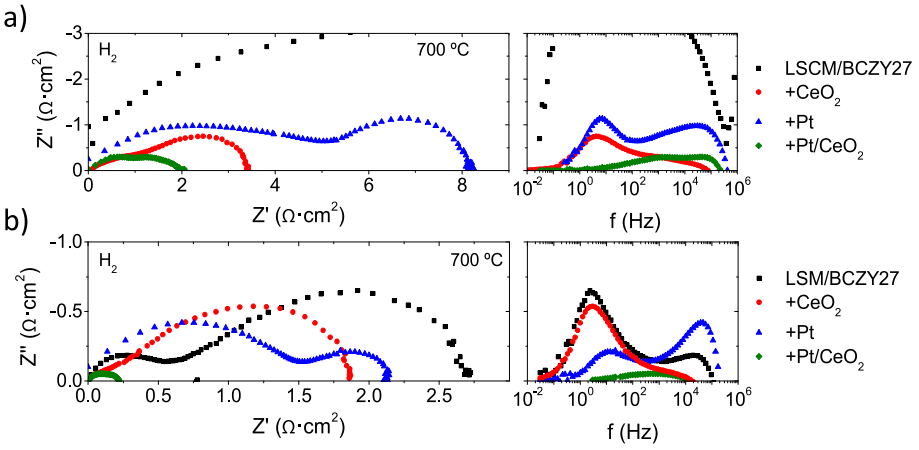

Fig. 6. EIS spectra (Nyquist and Bode plot) for the composite electrodes LSCM/BCZY27 (a), LSM/BCZY27 (b) and LSCM/BCZY27, LSM/BCZY27 electrodes infiltrated with CeO_2, Pt y Pt/CeO_2 at 700 °C measured under humidified 50% H_2 in Ar. Ohmic resistances were subtracted for clarity reasons.

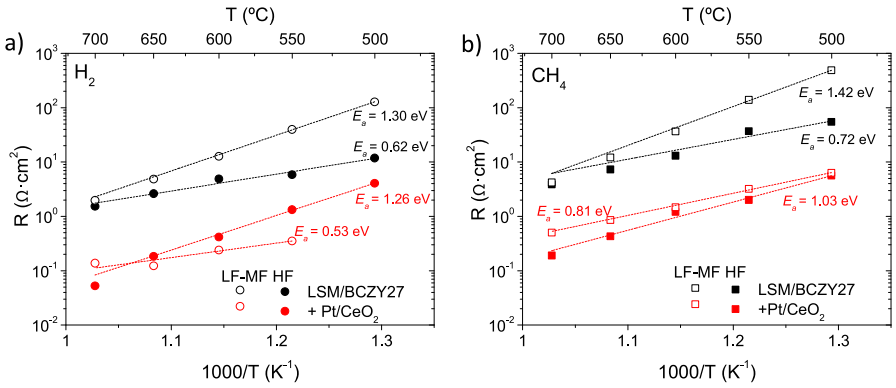

Fig. 7. Contributions of the LF + MF and HF resistances of LSM/BCZY27 and LSM/BCZY27 electrodes infiltrated with Pt/CeO_2 cells as a function of temperature under humidified 50% H_2 in Ar (a) and 9% CH_4-10% H_2 in Ar (b).

atmosphere, which can be expected since LSM is the state-of-the-art cathode material for high temperature SOFCs [36]. It is well known that the oxygen vacancies concentrations are very low and thus, mixed conductivity contributes minimally to the performance of the electrodes.

On the other hand, it should be outlined that very low polarization resistance values were measured for the LSM/BCZY27 infiltrated with Pt/CeO_2, 0.19 Ω cm^2 in 50% H_2 and 0.70 Ω cm^2 in 9% CH_4-10% H_2 in Ar at 700 °C, which can be attributed to an improved catalytic promotion if both catalysts are combined. R_p and E_a values for LSM/BCZY27 based electrodes at 700 °C are shown in Table 1. Regarding the activation energy, the Pt-infiltrated LSM/BCZY27 electrode presents the lowest values in H_2 and CH_4 atmospheres and the highest E_a in humidified synthetic air, if compared to the backbone, CeO_2 and Pt/CeO_2 infiltrated electrodes.

Overall, the same trends were observed as for the infiltrated LSCM/BCZY27 electrodes confirming the effect of the catalytic promotion of the different tested catalysts: (i) the addition of CeO_2 resulted in an improved electrochemical performance; (ii) the addition of Pt affects positively the electrochemical performance, mostly in O_2-containing atmospheres; and (iii) addition of Pt/CeO_2 improves further the performance, obtaining the lowest R_p values in both, H_2 and CH_4-containing atmospheres.

Nyquist and Bode plots for the LSCM/BCZY27 and LSM/BCZY27 backbones and the infiltrated electrodes are shown in Fig. 6a and b, respectively recorded at 700 °C in humidified 50% H_2. The impedance spectra of these electrodes were fitted to an equivalent circuit with three RQ-elements. As previously mentioned, non-infiltrated electrodes are limited by the low-frequency processes, classically related to surface-reaction processes. Here, it can be observed how the catalyst infiltration with CeO_2, Pt or Pt/CeO_2 improves the performance of the electrodes. More specifically, the LF + MF contributions decrease, which can be correlated to the increase in the number of active sites available for the electrochemical reaction to take place, through the surface dispersion of nanoparticles with higher intrinsic electrocatalytic activity.

Fig. 7 shows the resistance contributions as deconvoluted from impedance spectra from the best performing electrode, namely LSM/BCZY infiltrated with Pt/CeO_2 and the backbone LSM/BCZY for comparison, under both H_2- and CH_4-containing atmospheres. The spectra were deconvoluted into three arc contributions and, thus, the resistance is named high frequency (HF) contribution if the associated capacitance is lower than $\sim 5 \cdot 10^{-5}$ F/cm^2 and low-medium frequency (LF + MF) contributions for the others. Regarding the effect of the atmosphere, the LSM/BCZY backbone shows smaller polarization resistance values and lower activation energies in humidified 50% H_2 in Ar with a similar behaviour for both contributions, indicating a limitation of the LF + MF contribution, as the LF + MF values are larger than the HF ones. High-frequency capacitances are of 10^{-7}-10^{-6} F/cm^2 and low-medium frequency capacitances of 10^{-3}-1 F/cm^2. On the other hand, the infiltrated LSM/BCZY shows a decrease in both contributions together with a change in the activation energies. The introduction of Pt/CeO_2 reduces the LF + MF contribution, which was limiting, and its activation energy, evidencing the surface-related nature of the LF + MF processes. Furthermore, the capacitance associated to the LF + MF contributions of the infiltrated electrodes is 10^{-4}-10^{-2} F/cm^2, demonstrating an enhancement of the surface steps and a faster surface exchange kinetics, since the processes are shifted to higher frequencies. The HF resistance of the infiltrated electrodes associated to the electrode-electrolyte interfacial processes (10^{-7}-10^{-5} F/cm^2), also decreases showing that the protonic transport at the interface also contributes to the overall electrode performance.

The performance of the infiltrated electrodes under CH_4-containing atmospheres (wet 9% CH_4 and 10% H_2 in Ar) at 700 °C was evaluated for 24 h by continuously carrying out EIS measurements. The obtained polarization resistance values as a function of time are plotted in Fig. 8.

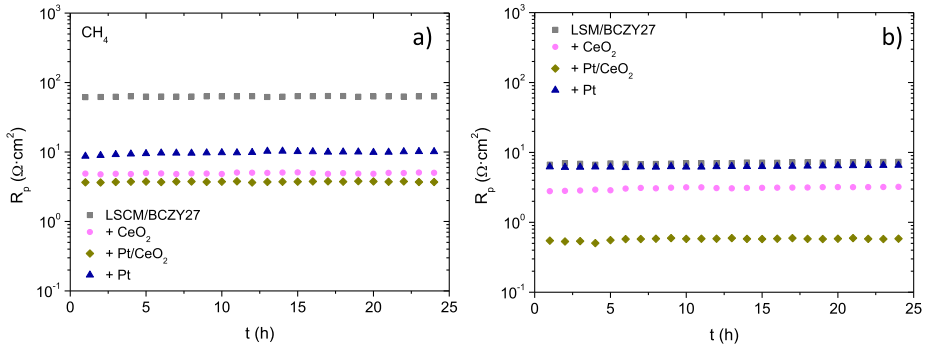

Fig. 8. Polarization resistance as a function of time for LSCM/BCZY27 (a), LSM/BCZY27 (b) and LSCM/BCZY27, LSM/BCZY27 electrodes infiltrated with CeO_2, Pt y Pt/CeO_2 at 700 °C measured under humidified 9% CH_4 and 10% H_2 in Ar.

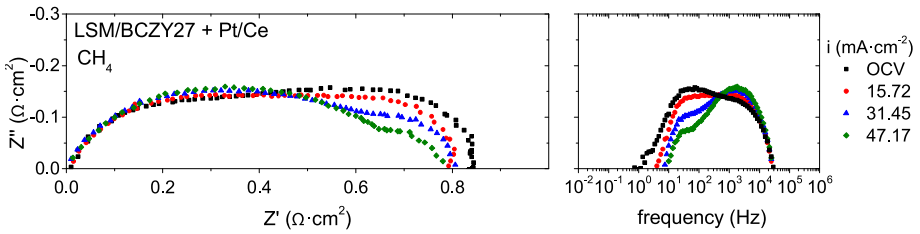

Fig. 9. Effect of the imposed current on LSM/BCZY27 infiltrated with Pt/CeO_2: Nyquist and Bode plots measured at 700 °C under humidified 9% CH_4 and 10% H_2 in Ar.

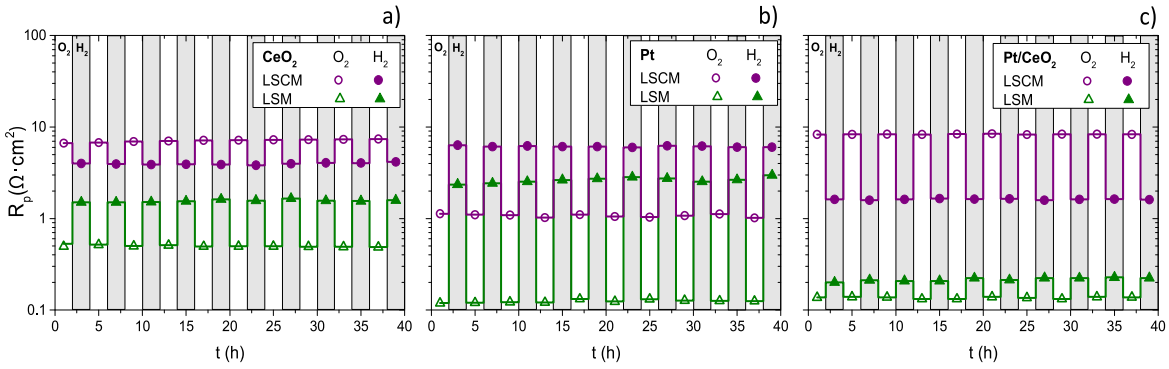

Fig. 10. Redox stability cycles (humidified synthetic air – humidified 50% H_2 in Ar) at 700 °C for the infiltrated composite electrodes LSCM/BCZY27 and LSM/BCZY27 with CeO_2 (a), Pt (b) and Pt/CeO_2 (c).

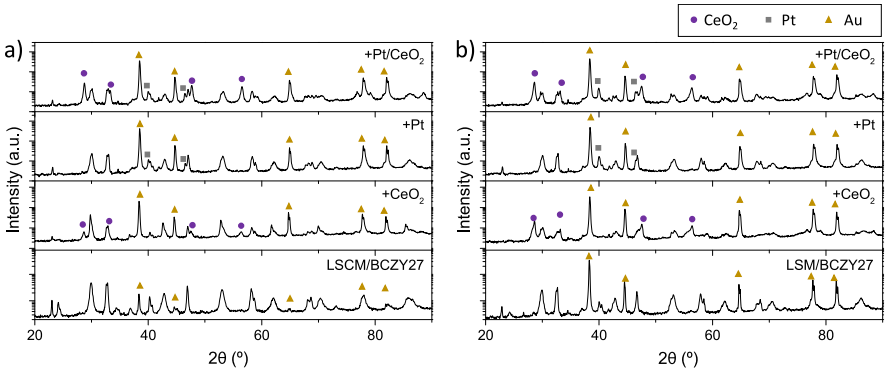

Fig. 11. XRD of the composite backbone LSCM/BCZY27 infiltrated with CeO_2, Pt and Pt/CeO_2 (a) and LSM/BCZY27 infiltrated with CeO_2, Pt and Pt/CeO_2 (b), respectively, after the electrochemical testing.

No evidence of degradation in the electrodes was observed during this treatment.

Fig. 9 shows the effect of the imposed current on the performance of the LSM/BCZY27 infiltrated with Pt/CeO_2. Two different contributions (MF and HF) can be distinguished, with a significant decrease of the MF when the current was applied. The nearly constant HF indicates that the transport properties are preserved while the application of current density mostly affects the surface (gas-solid interface) processes.

The capacitance associated with MF processes after modelling using the equivalent circuit $LR_0(R_{HF}CPE_{HF})(R_{MF}CPE_{MF})$ is around 10^{-1} F/cm^2.

Fig. 10 shows nine consecutive redox cycles carried out changing from humidified synthetic air to humidified 50% H_2 in Ar at 700 °C for the infiltrated composite electrodes LSCM/BCZY and LSM/BZCY. For LSCM based electrodes, it is seen that polarization losses are larger in oxidizing atmospheres if infiltrated with CeO_2 and Pt/CeO_2. In contrast, infiltrated LSM/BCZY showed lower losses in O_2-containing atmospheres. The largest difference between oxidizing and reducing atmospheres is found if the electrodes are infiltrated with Pt. Overall, regenerative redox capacity and no degradation are observed for all the catalytic activated composite electrodes tested. The lowest polarization resistance values in both humidified O_2- and H_2-containing atmospheres and the lowest difference variation is achieved for the LSM/BZCY electrode infiltrated with Pt/CeO_2, revealing promising properties as redox-stable electrodes.

The post-mortem cells were structurally characterized by XRD and SEM after the electrochemical measurements in H_2 and CH_4 and the consecutive redox cycling. XRD patterns of the infiltrated LSCM/BCZY27 and LSM/BCZY27 are shown in Fig. 11. Both porous infiltrated backbones present the corresponding phases of the infiltrated nanoparticles, either CeO_2, Pt or Pt/CeO_2, with no evidence of impurities or additional secondary phases. The presence of Au is due to the printed current-collector mesh.

3.4. Chemical compatibility with CH_4 and aromatics

For application of these redox-stable electrodes in reactions such as

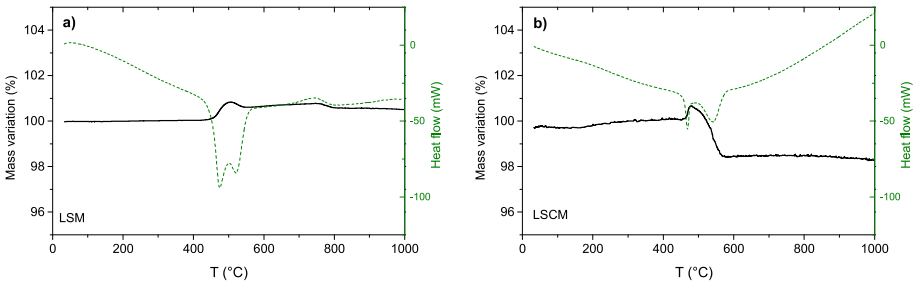

Fig. 12. TGA and DSC analysis of LSCM and LSM in synthetic air after a treatment in CH_4 saturated in toluene at 800 °C for 1 h to study the coke formation.

MDA (methane dehydroaromatization) and SMR (steam methane reforming), electrodes should not promote the coke formation under atmospheres containing CH_4, light olefins and/or aromatics. In order to study the potential coke formation, LSCM and LSM were treated in pure CH_4 saturated in toluene at 800 °C for 1 h and after that, coke formation was evaluated by TGA measurements and DSC analysis under synthetic air (Fig. 12). Both materials present a mass gain followed by a weight loss at the same temperature range. The initial mass gain is ascribed to the oxidation of the materials, while the main mass loss is correlated with the coke formed during the treatment with CH_4 and toluene. Thus, the quantification of the main mass loss (gC/g_{mat}) is ascribed to the carbonaceous species (coke) formed on each material. In the case of LSCM 0.022 gC/g_{mat} were formed whereas for LSM was 0.023 gC/g_{mat}. It should be noted that all carbonaceous species are oxidized below 550 °C which is attributed to amorphous carbon, which implies an easier and quicker regeneration compared to filamentous carbon and graphite which require higher oxidation temperatures (>600 °C).

4. Conclusions

In this work, the chemical compatibility of four different perovskite materials ($La_{0.85}Sr_{0.15}FeO_3$ (LSF8515), $La_{0.5}Sr_{0.5}FeO_3$ (LSF55), $La_{0.8}Sr_{0.2}Cr_{0.5}Mn_{0.5}O_3$ (LSCM) and $La_{0.8}Sr_{0.2}MnO_3$ (LSM)) with the protonic electrolyte material $BaCe_{0.2}Zr_{0.7}Y_{0.1}O_{3-\delta}$ (BCZY27) was studied. Microstructural and electrochemical properties of the composites revealed LSCM/BCZY27 and LSM/BCZY27 as the best performing electrodes in both humidified H_2 and CH_4 atmospheres. Further electrode improvement of the electrochemical performance and stability upon redox cycling (humidified air – humidified H_2) was achieved by infiltration of Pt, CeO_2 and binary Pt/CeO_2 nanoparticles. The best electrochemical performance was obtained for the LSM/BCZY27 electrode infiltrated with the binary Pt/CeO_2 revealing a synergetic effect between both components. In addition, the stability and coke formation of LSCM and LSM powders were investigated under atmospheres containing CH_4 and aromatics. Taking into account the excellent electrochemical performance, redox-cyclability and stability over time, it can be concluded that the catalytically-activated LSCM and LSM are solid electrode candidates enabling electrochemically-promoted catalytic reactions involving non-oxidative hydrocarbon upgrading and redox-regenerative cycling.

CRediT authorship contribution statement

L. Almar: Investigation, Methodology, Formal analysis, Data curation, Project administration, Writing – original draft, Writing – review & editing. **N. Bausá:** Investigation, Methodology, Formal analysis, Data curation, Writing – review & editing. **M. Fabuel:** Resources, Investigation. **S. Escolástico:** Investigation, Conceptualization, Writing – original draft, Project administration, Supervision. **J.M. Serra:** Conceptualization, Conceptualization, Supervision, Writing – review & editing, Supervision, Funding acquisition.

Declaration of competing interest

The authors declare that they have no known competing financial interests or personal relationships that could have appeared to influence the work reported in this paper.

Data availability

Data will be made available on request.

Acknowledgements

Part of the present research was developed in the frame of N. Bausá's PhD thesis (Chapter 9) that has received funding from Spanish Government (RTI2018-102161 grant). This work has been also supported by the WINNER project. This project has received funding from the Fuel Cells and Hydrogen 2 Joint Undertaking (now Clean Hydrogen Partnership) under Grant Agreement No 101007165. This Joint Undertaking receives support from the European Union's Horizon 2020 Research and Innovation program, Hydrogen Europe and Hydrogen Europe Research.

References

[1] F. Gallucci, E. Fernandez, P. Corengia, M. van Sint Annaland, Recent advances on membranes and membrane reactors for hydrogen production, Chem. Eng. Sci. 92 (2013) 40–66.
[2] T. Boeltken, A. Wunsch, T. Gietzelt, P. Pfeifer, R. Dittmeyer, Ultra-compact microstructured methane steam reformer with integrated Palladium membrane for on-site production of pure hydrogen: experimental demonstration, in: International Journal of Hydrogen Energy, vol. 39, Elsevier Ltd, 2014, pp. 18058–18068.
[3] C. Duan, J. Huang, N. Sullivan, R. O'Hayre, Proton-conducting oxides for energy conversion and storage, Appl. Phys. Rev. 7 (2020), 011314.
[4] D. Clark, et al., Single-step hydrogen production from NH3, CH4, and biogas in stacked proton ceramic reactors, Science 376 (2022) 390–393.
[5] H. Malerød-Fjeld, et al., Thermo-electrochemical production of compressed hydrogen from methane with near-zero energy loss, Nat. Energy 2 (2017) 923–931.
[6] S.H. Morejudo, et al., Direct conversion of methane to aromatics in a catalytic co-ionic membrane reactor, Science 353 (2016) 563–566 (80-.).
[7] J. Gao, et al., Identification of molybdenum oxide nanostructures on zeolites for natural gas conversion, Science 348 (2015) 686–690 (80-.).
[8] Y. Xu, X. Bao, L. Lin, Direct conversion of methane under nonoxidative conditions, in: Journal of Catalysis, vol. 216, Academic Press Inc., 2003, pp. 386–395.
[9] C.H.L. Tempelman, E.J.M. Hensen, On the deactivation of Mo/HZSM-5 in the methane dehydroaromatization reaction, Appl. Catal. B Environ. 176–177 (2015) 731–739.
[10] Y. Yu, et al., BaZr0.1Co0.4Fe0.4Y0.1O3-SDC composite as quasi-symmetrical electrode for proton conducting solid oxide fuel cells, Ceram. Int. 46 (2020) 11811–11818.
[11] D. Kim, S.J. Son, M. Kim, H.J. Park, J.H. Joo, PrBaFe2O5+δ promising electrode for redox-stable symmetrical proton-conducting solid oxide fuel cells, J. Eur. Ceram. Soc. 41 (2021) 5939–5946.
[12] L.R. Tarutina, et al., Doped (Nd,Ba)FeO3 oxides as potential electrodes for symmetrically designed protonic ceramic electrochemical cells, J. Solid State Electrochem. 24 (2020) 1453–1462.
[13] J. Lu, et al., Highly efficient electrochemical reforming of CH4/CO2 in a solid oxide electrolyser, Sci. Adv. 4 (2018).
[14] G. Xiao, F. Chen, Redox stable Anodes for solid oxide fuel cells, Front. Energy Res. 2 18 (2014).
[15] S. Tao, J.T.S. Irvine, A redox-stable efficient anode for solid-oxide fuel cells, Nat. Mater. 2 (2003) 320–323.
[16] J.C. Ruiz-Morales, D. Marrero-López, J. Canales-Vázquez, J.T.S. Irvine, Symmetric and reversible solid oxide fuel cells, RSC Adv. (2011) 1 1403–1414.

[17] D.M. Bastidas, S. Tao, J.T.S. Irvine, A symmetrical solid oxide fuel cell demonstrating redox stable perovskite electrodes, J. Mater. Chem. 16 (2006) 1603–1605.
[18] C. Graves, S.D. Ebbesen, S.H. Jensen, S.B. Simonsen, M.B. Mogensen, Eliminating degradation in solid oxide electrochemical cells by reversible operation, Nat. Mater. 14 (2015) 239–244.
[19] N. Bausá, C. Solís, R. Strandbakke, J.M. Serra, Development of composite steam electrodes for electrolyzers based on barium zirconate, Solid State Ionics 306 (2017) 62–68.
[20] N. Bausá, J.M. Serra, Robust catalytically-activated LSM-BCZY-based composite steam electrodes for proton ceramic electrolysis cells, RSC Adv. 9 (2019) 20677–20686.
[21] N. Bausá, S. Escolástico, J.M. Serra, Direct CO_2 conversion to syngas in a $BaCe_{0.2}Zr_{0.7}Y_{0.1}O_{3-\delta}$-based proton-conducting electrolysis cell, J. CO2 Util. 34 (2019).
[22] D. Ding, X. Li, S.Y. Lai, K. Gerdes, M. Liu, Enhancing SOFC cathode performance by surface modification through infiltration, Energy Environ. Sci. 7 (2014) 552.
[23] J.M. Serra, H.P. Buchkremer, On the nanostructuring and catalytic promotion of intermediate temperature solid oxide fuel cell (IT-SOFC) cathodes, J. Power Sources 172 (2007) 768–774.
[24] S.P. Jiang, Nanoscale and nano-structured electrodes of solid oxide fuel cells by infiltration: advances and challenges, Int. J. Hydrog. Energy 37 (2012) 449–470.
[25] L. Navarrete, C. Solís, J.M. Serra, Boosting the oxygen reduction reaction mechanisms in IT-SOFC cathodes by catalytic functionalization, J. Mater. Chem. 3 (2015) 16440–16444.
[26] H. Shimada, et al., Nanocomposite electrodes for high current density over 3 A cm−2 in solid oxide electrolysis cells, Nat. Commun. 10 (2019).
[27] K.K. Hansen, Evaluation of LSF based SOFC cathodes using cone-shaped electrodes and EIS, Solid State Ionics 344 (2020), 115096.
[28] S. Tao, J.T.S. Irvine, Phase transition in perovskite oxide La0.75Sr0.25Cr0.5Mn0.5O3-δ observed by in situ high-temperature neutron powder diffraction, Chem. Mater. 18 (2006) 5453–5460.
[29] F. Tietz, I. Arul Raj, M. Zahid, D. Stöver, Electrical conductivity and thermal expansion of La0.8Sr0.2(Mn,Fe,Co)O3-δ perovskites, Solid State Ionics 177 (2006) 1753–1756.
[30] J.S. Fish, et al., Synthesis by spark plasma sintering of a novel protonic/electronic conductor composite: BaCe0.2Zr0.7Y0.1O3−δ/Sr0.95Ti0.9Nb0.1O3−δ(BCZY27/STN95), J. Mater. Sci. 48 (2013) 6177–6185.
[31] X. Luo, et al., Reduced-temperature redox-stable LSM as a novel symmetrical electrode material for SOFCs, Electrochim. Acta 260 (2018) 121–128.
[32] Y.-W. Sin, V. Petrovsky, H.U.U. Anderson, Redox stable electrodes for hydrogen producing solid oxide electrolyzer, ECS Trans. 2 (2007) 1–7.
[33] M.V. Patrakeev, et al., Electron/hole and ion transport in La1-xSrxFeO3-δ, J. Solid State Chem. 172 (2003) 219–231.
[34] M.D. Anderson, J.W. Stevenson, S.P. Simner, Reactivity of lanthanide ferrite SOFC cathodes with YSZ electrolyte, J. Power Sources 129 (2004) 188–192.
[35] J. Kong, Y. Zhang, C. Deng, J. Xu, Synthesis and electrochemical properties of LSM and LSF perovskites as anode materials for high temperature steam electrolysis, J. Power Sources 186 (2009) 485–489.
[36] S.P. Jiang, Development of lanthanum strontium manganite perovskite cathode materials of solid oxide fuel cells: a review, J. Mater. Sci. 43 (2008) 6799–6833.